1   **Revision 2**

2   **High-pressure phase behavior and equations of state of ThO₂ polymorphs**

3   **Authors:** Bethany A. Chidester[1,*,†], Olivia S. Pardo[1,††], Rebecca A. Fischer[1,†††], Elizabeth

4   C. Thompson[1], Dion L. Heinz[1], Clemens Prescher[2,††††], Vitali B. Prakapenka[2], and

5   Andrew J. Campbell[1]

6   **Affiliations:** [1]Department of the Geophysical Sciences, University of Chicago, Chicago,

7   IL 60637

8   [2]GeoSoilEnviroCARS, University of Chicago, Argonne National Laboratory, Argonne,

9   IL 60439

10   [†]Present address: Earth and Planetary Sciences Department, University of California

11   Davis, Davis, CA 95616

12   [††]Present address: Division of Geological and Planetary Sciences, California Institute of

13   Technology, Pasadena, CA 91125

14   [†††]Present address: Department of Earth and Planetary Sciences, Harvard University,

15   Cambridge, MA 02138

16   [††††]Present address: Institut für Geologie und Mineralogie, Universität zu Köln, 50674

17   Köln, Germany

18   *Email: bchides@sandia.gov

19

23

ABSTRACT

ThO_2 is an important material for understanding the heat budget of Earth's mantle, as well as the stability of nuclear fuels at extreme conditions. We measured the in situ high-pressure, high-temperature phase behavior of ThO_2 to ~60 GPa and ~2500 K. It undergoes a transition from the cubic fluorite-type structure (thorianite) to the orthorhombic α-$PbCl_2$ cotunnite-type structure between 20 and 30 GPa at room temperature. Prior to the transition at room temperature, an increase in unit cell volume is observed, which we interpret as anion sub-lattice disorder or pre-transformation "melting" (Boulfelfel et al., 2006). The thermal equation of state parameters for both thorianite ($V_0 = 26.379(7)$, $K_0 = 204(2)$, $\alpha K_T = 0.0035(3)$)) and the high-pressure cotunnite-type phase ($V_0 = 24.75(6)$, $K_0 = 190(3)$, $\alpha K_T = 0.0037(4)$)) are reported, holding K_0' fixed at 4. The similarity of these parameters suggests that the two phases behave similarly within the deep Earth. The lattice parameter ratios for the cotunnite-type phase change significantly with pressure, suggesting a different structure is stable at higher pressure.

INTRODUCTION

Actinides, specifically U and Th, are important in the Earth as long-lived radioactive heat producing elements. Assuming the refractory lithophile element budget of the bulk silicate Earth is chondritic in composition, these elements produce up to 36% of the total heat fluxed out of the planet's surface, but their distribution and role within the dynamics of the deepest part of Earth's mantle is unknown (McDonough and Sun, 1995). These elements are highly refractory (ThO_2 has the highest melting temperature of any oxide at ambient pressures at 3663 K) and nominally incompatible in major mantle

2

47   minerals, meaning they tend to partition into melts or accessory phases, which makes

48   them excellent tracers for chemical reservoirs in the deep Earth as well as within other

49   planetary bodies (Arevalo Jr. et al., 2009; Fonseca et al., 2014). Additionally, U and Th

50   and their oxides are increasingly important as nuclear energy sources for our growing

51   population and they are used in thermally resistant ceramics (Cuney, 2013). However,

52   stable materials that resist decomposition or amorphization under varying pressure,

53   temperature, and radiation conditions are needed to contain and immobilize the resulting

54   waste from this industrial usage. Actinide-bearing minerals that are stable under a variety

55   of thermodynamic conditions can point to analogous materials that are stable at ambient

56   conditions. Thus, exploring the mineralogy of actinide-bearing minerals at the extreme

57   pressure and temperature conditions of Earth's mantle (tens of gigapascals and thousands

58   of Kelvin) is universally important. This paper focuses on the high-pressure, high-

59   temperature phase behavior and equations of state of the simplest Th-bearing mineral,

60   ThO_2.

61   End-member ThO_2 (thorianite) takes the cubic fluorite-type (CaF_2, $Fm3m$)

62   structure at ambient conditions (Fig. 1a). Room temperature X-ray diffraction (XRD)

63   studies show that upon compression this material undergoes a reconstructive phase

64   transition to the orthorhombic cotunnite-type structure (α-$PbCl_2$, $Pnma$) (Fig. 1b)

65   (Dancausse et al., 1990; Idiri et al., 2004; Jayaraman et al., 1988; Olsen et al., 2004). This

66   phase transition results in an increase in coordination number of the Th cation, from 8-

67   fold (cubic) in the fluorite-type structure to 9-fold in the cotunnite-type structure. At

68   room temperature, this phase transition is kinetically inhibited, with the high-pressure

69   phase first appearing between 30-40 GPa, and coexisting with the metastable low-

3

70　pressure phase until 55-57 GPa when the transition is observed to be complete. Because

71　of this sluggishness, the precise position of the equilibrium phase boundary is not well

72　constrained.

73　　　　Materials in the fluorite-type structure, including ThO_2, have been shown to

74　undergo a "superionic" transition at about 80% the melting temperature of the material,

75　whereby a critical concentration of Frenkel defects occur in the crystal, resulting in anion

76　sub-lattice "melting" (Clausen et al., 1989; Kuksin and Smirnova, 2014; Kupryazhkin et

77　al., 2011; March et al., 1980; Matveev and Veshchunov, 1997). This transition includes

78　an exponential increase in the enthalpy and specific heat of the material. One

79　computational study has suggested that this transition also occurs at ambient temperature

80　under increasing pressure in the type specimen of fluorite, CaF_2 (Boulfelfel et al., 2006).

81　In this case, the formation of a Frenkel defect, in which a F^- anion shifts from its

82　tetrahedral site to a previously empty octahedral site, allowing another F^- anion to take its

83　place, locally expands the lattice and allows the Ca cations to subsequently shift to their

84　new crystallographic position in the cotunnite-type structure at high pressures.

85　　　　Previous experiments have shown that phase transitions in similar systems, such

86　as some of the rare Earth pyrochlore ($A_2Zr_2O_7$)/defect-fluorite (($A,Zr)_4O_7$) zirconate

87　materials, which often undergo either amorphization or structural transition to the (defect)

88　cotunnite-type structure under pressure, exhibit anomalous volume expansion just prior to

89　the phase transition (Rittman et al., 2017; Zhang et al., 2010). However, this volume

90　expansion has not been recognized universally in other pyrochlore systems (Li et al.,

91　2016; Rittman et al., 2017). It is likely that the anions in these more complicated

92　pyrochlore compounds are undergoing a similar distortion to the one described above for

93   CaF$_2$, although it may be dependent upon the relative radii of the cations in the A and B

94   sites (Rittman et al., 2017). A recent Raman spectroscopy study on bulk ThO$_2$ under

95   pressure has suggested that this material also experiences anion sub-lattice disorder at

96   high pressures (Kamali et al., 2017). It was recognized in that study that one Raman

97   mode appeared within the ThO$_2$ spectrum at ~25 GPa as shoulder on the F$_{2g}$ mode of

98   fluorite-type ThO$_2$, approximately 10 GPa lower than the rest of the cotunnite-type

99   modes appeared in the spectrum (~37 GPa). This mode is thought to signal anion disorder

100   since the F$_{2g}$ mode results from the breathing of O anions around the Th cation, thus it is

101   only sensitive to movements of the O atoms. UO$_2$ also exhibits shoulders on the F$_{2g}$ peak,

102   which are thought to be related to anion sub-lattice disorder, but in this case the disorder

103   may be enhanced due to a slight excess of O in the structure (hyperstoichiometry)

104   (Crowhurst et al., 2015).

105   The thermo-elastic parameters (e.g. bulk modulus, K, and thermal expansion, α)

106   of this material are necessary for describing its thermodynamic behavior at extreme

107   conditions of pressure and temperature. Recent measurements (XRD, ultrasonic) and

108   calculations of the ambient-pressure isothermal bulk modulus (K_0) of pure thorianite at

109   300 K are consistent around 185-198 GPa with a pressure derivative (dK/d$P = K_0'$, where

110   relevant) of ~5 (Boettger, 2009; Boudjemline et al., 2011; Idiri et al., 2004; Kanchana et

111   al., 2006; Li et al., 2014; Macedo et al., 1964; Olsen et al., 2004; Shein et al., 2007; Wang

112   et al., 2010). Earlier XRD studies resulted in much higher values of K_0 and K_0' - 262 GPa

113   and 6.7, respectively (Dancausse et al., 1990), while an inelastic X-ray scattering

114   experiment and a different series of calculations predicted K_0 values around 220 GPa

115   (Clausen et al., 1989; Kanchana et al., 2006; Li et al., 2002; Olsen et al., 2004; Sevik and

5

116   Çağın, 2009). These results are summarized in Table 1. To date, no experimental studies

117   have reported on the behavior of this material at simultaneous high pressures and high

118   temperatures or on the equation of state of the high-pressure cotunnite-type phase.

119   Calculations of the elastic parameters of the high-pressure phase are inconsistent, ranging

120   in values between K_0 = 148-207 and $K_0{'}$ = 4.2-7.8 (Boettger, 2009; Boudjemline et al.,

121   2011; Li et al., 2014; Wang et al., 2010). In this study, we conducted in situ XRD

122   measurements of ThO_2 to ~60 GPa and ~2500 K to more precisely define the thorianite–

123   cotunnite-type phase boundary and to measure the thermal equation of state parameters

124   for both the low- and high-pressure phases of this material.

125

126   **SYNCHROTRON X-RAY DIFFRACTION AND RAMAN SPECTROSCOPY**

127   **EXPERIMENTS**

128   Four synchrotron powder X-ray diffraction (XRD) experiments on ThO_2 were

129   conducted in the laser-heated diamond anvil cell (LH-DAC), with diamond culets of 300

130   μm or 250 μm. ThO_2 (99.99%) was purchased from Strem Chemical. The ThO_2 starting

131   material was characterized by an ambient condition XRD measurement at the University

132   of Chicago using incident radiation of λ = 1.5418 Å (Cu K_α) and Si powder (NBS 640a)

133   as an X-ray standard. In high P-T experiments, amorphous Pt (Alfa Aesar, 0.2-1.6 μm,

134   99.9%) was mixed with the ThO_2 as an absorber for laser heating. The ThO_2/Pt mixture

135   was loaded as a powder between flakes of KCl (reagent grade, Alfa Aesar) or KBr

136   (spectroscopy grade, Alfa Aesar), which acted as the pressure medium, thermal insulator

137   and pressure standard in the high-temperature experiments (Dewaele et al., 2012).

138   Sample B12 was measured at room temperature using cryogenically-loaded Ar as the

6

139   pressure medium and pressure standard (Ross et al., 1986). A 3% uncertainty was

140   assigned to the accuracy of the Ar pressure standard.

141   Following safety regulations for radiogenic samples at the Department of Energy

142   facilities where these measurements were made, experiments used double containment to

143   prevent accidental environmental contamination or dispersal. The gasket and diamonds

144   provided the first layer of containment. For the second layer of containment, the DACs

145   were securely wrapped in Kapton® tape around the diameter of the cell. In the laser-

146   heating path, thin (0.5 mm) sapphire windows (6.35 mm diameter, Edmund Optics) were

147   adhered to the outside of the diamond seat by epoxy. The sapphire windows typically

148   resulted in several large and distinctive X-ray diffraction spots on the detector, which

149   were masked during data analysis.

150   Room temperature angle-dispersive powder XRD experiments were performed at

151   sector 12.2.2 at the Advanced Light Source (ALS), Lawrence Berkeley National

152   Laboratory, using a monochromatic incident X-ray beam ($\lambda = 0.4959$ Å) of ~10 μm in

153   diameter. High-temperature XRD experiments were conducted at sector 13-ID-D (GSE-

154   CARS) of the Advanced Photon Source (APS), Argonne National Laboratory, using a

155   monochromatic incident X-ray ($\lambda = 0.3344$ Å) typically measuring ~3 x 4 μm. At both

156   facilities, sample to detector distance and tilt were calibrated using LaB_6. High-

157   temperature samples were compressed to a target pressure and laser heated while XRD

158   measurements were simultaneously collected. The heating laser was co-aligned with the

159   X-ray beam using the X-ray induced fluorescence of the KCl or KBr insulator. Laser-

160   heating was done from both sides of the sample, adjusting upstream and downstream

161   laser power to balance the temperature. Surface temperatures were measured spectro-

162   radiometrically using the Plank radiation function (Prakapenka et al., 2008), and

163   corrected by -3% to account for the axial temperature gradient across the sample

164   (Campbell et al., 2007). The temperature of the alkali halide thermal insulator was

165   estimated as the midpoint between the surface of the sample and the surface of the

166   diamond anvil as described by Campbell et al. (2009).

167   Powder XRD patterns were collected on a CCD and azimuthally integrated to

168   intensity vs. 2θ (degrees) plots using DIOPTAS (Prescher and Prakapenka, 2015). Lattice

169   parameters as a function of pressure and temperature were determined by fitting

170   reflection positions using PeakFit (Systat Software). At least one XRD pattern per

171   heating cycle was fully indexed to confirm the space group and lattice parameters at each

172   pressure step using GSAS-II (Toby and Von Dreele, 2013) or DICVOL04 (Boultif and

173   Louër, 2004), which is part of the FULLProf Suite (Rodriguez-Carvajal, 1993).

174   In addition to XRD measurements, the room-temperature phase behavior of ThO_2

175   was investigated using Raman spectroscopy in the Laboratory for Mineral Physics at the

176   University of Chicago. Samples were prepared either as ThO_2 powder pressed between

177   two MgO flakes, which acted as a Raman-inactive pressure-transmitting medium, or

178   without a pressure medium. All samples were loaded in a steel gasket with an 80 µm

179   sample chamber and 300 µm culet DAC. Measurements were taken using a 0.75-meter

180   Acton SpectraPro monochromator with a 473 nm 150 mW blue laser. Pressure was

181   determined using the Raman shift of the diamond, which was calibrated to ruby under

182   quasi-hydrostatic conditions after Akahama and Kawamura (2007). Raman acquisitions

183   were centered at 712 cm^{-1} to minimize nearby diamond Raman interference and were the

184   average of 600 one-second exposures at full laser power. Compression measurements

185   began at 3-5 GPa and samples were incrementally brought to ~60 GPa before

186   decompressing to ambient pressure. Raman mode frequencies were determined by peak

187   fitting using PeakFit (Systat Software). The reported frequencies are an average of three

188   individual fits and the reported uncertainty is the corresponding standard deviation.

189

190   **RESULTS AND DISCUSSION**

191   **Phase diagram ThO$_2$**

192   The measured lattice parameters and pressure-volume-temperature (P-V-T) data

193   points from the in situ XRD experiments are listed in Supplemental Table 1 (thorianite)

194   and Supplemental Table 2 (cotunnite-type ThO$_2$). Ambient pressure XRD measurement

195   of the ThO$_2$ starting material confirmed an initial fluorite-type structure (Fig. 1a) with a

196   lattice parameter of $a = 5.5958 \pm 0.0005$ Å ($V_0 = 26.379 \pm 0.007$ cm^3/mole), consistent

197   with literature values for end-member thorianite (Table 1). As with previous studies,

198   synchrotron XRD measurements at high pressure and room temperature demonstrate that

199   thorianite exists in this fluorite-type structure until ~34 GPa, at which point new

200   diffraction peaks appear between the (111) and (200) fluorite peaks, indicating the

201   emergence of the cotunnite-type phase, illustrated in Fig. 1b (Dancausse et al., 1990; Idiri

202   et al., 2004; Jayaraman et al., 1988; Olsen et al., 2004). Figure 2 shows high-temperature

203   examples of raw diffraction images and their corresponding integrated spectra (intensity

204   vs. 2θ) for this phase transition, as well as a higher P-T pattern containing only the

205   cotunnite-type phase.

206   The fluorite–cotunnite phase transition requires a crystallographic reconstruction,

207   which is characterized by a large degree of kinetic inhibition. As with previous XRD

9

208   measurements at room temperature, the fluorite-type phase was present up to the highest

209   pressures achieved at room temperature in this study, ~54 GPa (Dancausse et al., 1990;

210   Idiri et al., 2004; Olsen et al., 2004). This kinetic barrier has been previously observed in

211   room temperature compression studies using different techniques. Using Raman

212   spectroscopy, Jayaraman et al. (1988) observed the initiation of the phase transition

213   between 30 and 37 GPa, but did not reach high enough pressures to observe the

214   disappearance of the fluorite-type phase. The slight differences in the observed transition

215   pressure range in these studies (i.e. 54-57 GPa) are likely due to the use of different

216   pressure-transmitting media. Klotz et al. (2009) have measured the hydrostatic limits, as

217   well as the standard deviation from true pressure (calibrated to ruby) across the sample

218   chamber over a wide range of pressures for all of the pressure media used in the studies

219   described here. Our study used Ar as the room-temperature pressure medium, which is

220   more hydrostatic (i.e. exhibits a lower standard deviation from true pressure) at these

221   pressures and allows for a greater range of metastability than the pressure media in

222   previous studies, silicone oil, N_2, or 16:3:1 methanol:ethanol:water (Dancausse et al.,

223   1990; Idiri et al., 2004; Klotz et al., 2009; Olsen et al., 2004). The less hydrostatic

224   conditions in these studies created higher strains, resulting in more abrupt phase

225   transitions compared to the more hydrostatic conditions reported here.

226   In the room temperature volume vs. pressure (*V-P*) XRD data from this study and

227   those from the literature (Fig. 3), a discontinuity in compression behavior is observed

228   around ~16 GPa, similar to the discontinuities observed previously in other fluorite-type

229   and pyrochlore materials at high pressures (Rittman et al., 2017; Zhang et al., 2010).

230   Although the crystal structure remains in the fluorite-type phase above this pressure, the

10

231   measured volume is greater than expected by normal compressibility. We interpret this as

232   evidence of anion sub-lattice disorder in ThO_2 (Boulfelfel et al., 2006).

233   As described in the Introduction, during the fluorite–cotunnite transition the

234   anions are subject to local disordering, described by Boulfelfel et al. (2006) as "melting"

235   of the anionic sub-lattice. This effectively increases the local volume, and allows the

236   cations to subsequently rearrange. Thus, the change in compressibility is interpreted as

237   the onset of the fluorite–cotunnite phase transition. Our data show this discontinuity

238   much more intensely than the earlier literature data for ThO_2 (Idiri et al., 2004; Olsen et

239   al., 2004), which again is likely due to the differences in deviatoric stress conditions of

240   the measurements (Klotz et al., 2009). It is unclear whether this process is also evident in

241   the room temperature compression curve for the cotunnite-type phase because the room

242   temperature XRD patterns that contained that phase were not well enough resolved to

243   extract lattice parameters or volumes.

244   To further investigate this phase transition process, we performed Raman

245   spectroscopy at room temperature under non-hydrostatic conditions. As described in the

246   Methods section, measurements were made both on compression and decompression.

247   Examples of the compression spectra are shown in Fig. 4. Under these conditions,

248   thorianite exhibits a single (triply degenerate) Raman absorption mode representing the

249   symmetric breathing of the O anions around the Th cation (F_{2g}) at ~474 cm^{-1} at 5 GPa.

250   This peak broadens and shifts to higher wavelengths with increasing pressure throughout

251   the pressure range investigated. At ~22 GPa new peaks appear as a shoulder or very near

252   the F_{2g} peak at 540 (M1) and 622 (M2) cm^{-1}. Above 32 GPa a triplet of absorption modes

253   (M3-M5) become apparent at low wavenumbers, 330-390 cm^{-1} and a single peak

11

254   becomes resolvable at 495 cm^{-1} (M6). One final peak at ~330 cm^{-1} (M8) is resolved

255   above 50 GPa (Figs. 4 and 5). Group theory indicates that the cotunnite-type structure

256   should result in 18 distinct Raman modes. We observe 8 at the highest pressures reached.

257   Although our spectra are rather broad due to pressure effects, they are very similar to

258   those observed at ambient pressures in samples of cotunnite-type ZrO_2 and HfO_2

259   recovered from high pressures (Haines et al., 1997). The pressure dependence of these

260   high-pressure absorption frequencies is shown in Fig. 5 and tabulated, along with

261   calculated mode Grüneisen parameters in Table 2. Mode Grüneisen parameters describe

262   the volume dependence of the frequency of each individual vibrational mode. The

263   thermodynamic Grüneisen parameter is a weighted mean of all mode Grüneisen

264   parameters for the material, including the acoustic modes and other Raman-inactive

265   modes which were not probed in this study.

266   We interpret the additional peaks in the 20-30 GPa range as the rearrangement of

267   the anion sub-lattice, which is consistent with previous interpretations of Raman

268   measurements of ThO_2 (Kamali et al., 2017), although these limited data cannot be used

269   to determine the extent of disorder. The peaks appearing at 32 GPa are the final stages of

270   the fluorite–cotunnite phase transition. The vibrational modes exhibit a regular linear

271   slope as a function of pressure above 37 GPa. Thus, the full crystallographic

272   reconstruction of the cubic fluorite-type structure to the orthorhombic cotunnite-type

273   structure appears to be complete for both the anions and cations between 32 and 37 GPa.

274   This is approximately the pressure at which the cotunnite phase emerges in the room

275   temperature XRD data (Fig. 6) (Dancausse et al., 1990; Idiri et al., 2004; Olsen et al.,

276   2004). Since XRD is more sensitive to the Th atoms in this material, it appears that the

12

277   phase transition will not be evident using diffraction until a significant portion of the

278   cation sub-lattice has undergone transformation (i.e. above 32 GPa). Given the change in

279   slope of the Raman frequencies, none of the high-pressure modes appear to be directly

280   related to the low-pressure phase. Upon decompression, the cotunnite-type absorption

281   peaks remain until ~2 GPa while continually decreasing in Raman frequency. At ~1 GPa,

282   there is only a single peak remaining, at 463 cm^{-1}, suggesting that it has fully reverted

283   back to the fluorite-type structure.

284   The thorianite–cotunnite-type phase transition is also observed at high

285   temperatures. In synchrotron XRD experiments at ~17 GPa, the phase transition occurred

286   on increasing temperature between 1534 ± 114 K and 1583 ± 119 K. Again, this

287   transition is sluggish, even at high temperatures. The high-pressure phase was not

288   observed at all in the pressure step at ~18-19 GPa, which suggests that in those cases

289   heating was faster than the phase transition could proceed. Additionally, from 20-30 GPa

290   at high temperatures both phases are observed, but only one of them (likely the cotunnite-

291   type phase) can be thermodynamically stable. Above ~30 GPa at high temperatures, only

292   the cotunnite-type phase is observed up to the highest pressures reached in this study, ~62

293   GPa. All of this information was compiled as our preferred *P-T* phase diagram for this

294   material in Fig. 6. Based on our observations, it is likely that the phase boundary is very

295   close to vertical or slightly negative around 18-20 GPa in *P-T* space, although it is not

296   observed in the XRD data until ≥30 GPa.

297

298   **Equations of state of ThO₂ polymorphs**

13

299   Given the range of P-V-T data obtained for the polymorphs of ThO$_2$ in this study,

300   we were able to extract equation of state parameters for each phase. We fit both sets of

301   data to the Mie-Grüneisen type equations of state (eq. 1), where the reference pressure

302   (300 K) equation took the Birch-Murnaghan form (eq. 2).

303    $P = P_{300K} + P_{thermal}$ (1)

304    $P_{300K} = 3K_0 f (1 + 2f)^{\frac{5}{2}} \left(1 + \frac{3}{2} f (K_0' - 4)\right)$ (2)

305   Here, f is the finite Eularian strain, $\frac{1}{2}\left(\left(\frac{V}{V_0}\right)^{\frac{-2}{3}} - 1\right)$, V is the measured volume of the

306   material at pressure, P, V_0 is the ambient pressure volume, K_0 is the ambient pressure

307   isothermal bulk modulus, and K_0' is its pressure derivative. For the thorianite equation of

308   state, we only used the room temperature data prior to the volume discontinuity (<15

309   GPa). For the cotunnite-type phase, there were no room temperature patterns of high

310   enough quality to extract lattice parameters. Thus, no room temperature data were used in

311   the fits for the high-pressure phase. Because of the limited room temperature data, we

312   chose to define the thermal pressure as in equation 3.

313    $P_{thermal} = \alpha K_T (T - 300)$ (3)

314   α is thermal expansion and K_T is the bulk modulus at temperature, T. In this case, the

315   coefficient on temperature is taken to be constant.

316   The equation of state parameters for each phase are given in Table 1, along with

317   the available literature values. For thorianite, V_0 was measured prior to the compression

318   experiments to be 26.379(7) cm^3/mole, so it was fixed in the fitting routine. Additionally,

319   K_0' was fixed to a value of 4 to allow for more precise determination of the thermal term.

320   Our choice of 4 of K_0' is slightly lower than has previously been measured (~5), so our

14

321   measured bulk modulus is slightly higher at 204 GPa than other recent XRD studies (Idiri

322   et al., 2004; Olsen et al., 2004). The thermal pressure coefficient, αK_T, for thorianite was

323   determined to be 0.0035(3) GPa/K.

324   The properties of the high-pressure cotunnite-type phase of ThO_2 are very similar

325   to those of the low-pressure phase. Holding K_0' at a value of 4, the bulk modulus for this

326   phase was determined to be 190(3) GPa. This is slightly more compressible, but very

327   similar to the value for thorianite. Additionally, the thermal pressure coefficient was

328   found to be 0.0037(4) GPa/K, suggesting that the high-pressure phase reacts very

329   similarly to pressure and temperature as the low-pressure phase. The fitted zero-pressure

330   volume for the cotunnite-type phase is 24.75(6) cm^3/mole, which is 6.2% more dense

331   than thorianite at ambient conditions. This is virtually the same volume contrast that was

332   observed at ~35 GPa, by Idiri et al. (2004). The compiled *P-V-T* data from this study are

333   plotted in Fig. 7 along with calculated isotherms for comparison.

334   The values for the individual lattice parameters of the cotunnite-type phase are

335   given in the top panel of Fig. 8. Each one decreases with pressure, as expected, but the *a*-

336   axis appears to be compressing at a faster rate than either *b* or *c*, while the short *b*-axis

337   changes very little. This relationship is best demonstrated in the lattice parameter ratios as

338   a function of pressure in the lower panels of Fig. 8. In general, the ratios of the lattice

339   parameters change linearly with pressure, with only small dependencies on temperature.

340   This would occur if the coordination polyhedra within the cotunnite-type structure are

341   continuously distorting with pressure, and suggests that upon increasing compression the

342   material will undergo another structural phase transition. A transition of this type has

343   been predicted theoretically for ThO_2 above ~80 GPa by Perry et al. (2017). In the

15

344   calculation, the phase transition was signaled by a collapse in the *a*-axis and a

345   corresponding expansion of the *b*- and *c*-axes, which is consistent with the compression

346   behavior observed here. Some likely options for this higher pressure phase are common

347   post-cotunnite structures, including the hexagonal Fe_2P structure (P-62*m*) observed in the

348   ZrO_2 system (Nishio-Hamane et al., 2015) or the Ni_2In structure (*P6₃/mmc*) and

349   orthorhombic distortions thereof (Song et al., 2012). For convenience, the ratios have

350   been fitted to a linear dependence of pressure. The slopes and hypothetical zero-pressure

351   values from these fits are given in Table 3.

352

353   **IMPLICATIONS**

354   This study explores the simultaneous high-pressure, high-temperature behavior of

355   ThO_2. We find that the thorianite–cotunnite-type phase transition is kinetically inhibited,

356   even at 2000 K. The onset of the transition at room temperature begins at ~15-20 GPa, as

357   evidenced by an anomalously low compressibility of the cubic structure with pressure.

358   We interpret this change as anion sub-lattice disorder, which has been theoretically

359   predicted for the same phase transition in CaF_2 (Boulfelfel et al., 2006) and observed in

360   several analogous phase transitions in the pyrochlore/disordered fluorite system under

361   pressure (Rittman et al., 2017; Zhang et al., 2010). This transition pressure is

362   corroborated by Raman spectroscopy measurements (Figs. 4 and 5) (Jayaraman et al.,

363   1988; Kamali et al., 2017). At room temperature, the phase transition was not complete,

364   even at the highest pressures reached in this study, ~55 GPa. At high temperatures, the

365   onset of the phase transition was observed at ~18 GPa and was complete by ~30 GPa. If

366   Th exists in oxide form in the Earth's lower mantle, it is likely in a solid solution with

367   other large cations of +4 valence whose oxides also take the cotunnite structure, e.g.

368    $(Zr,Th,U)O_2$. Such a phase, with Zr as the dominant (i.e. most abundant) cation, could

369   exist in the cotunnite-type structure to at least ~1430 km (~60 GPa), as ZrO_2 has been

370   shown to be stable in the cotunnite-type structure well above this pressure (Nishio-

371   Hamane et al., 2015).

372   The isothermal equation of state parameters measured here for thorianite are

373   consistent with previous measurements (Idiri et al., 2004; Olsen et al., 2004).

374   Additionally, this study provides a thermal dependence for the high-pressure behavior of

375   thorianite, as well as thermal equation of state parameters for the high-pressure cotunnite-

376   type phase. These parameters are necessary for predicting the behavior of this material at

377   extreme conditions, such as within a nuclear reactor (a very high radiation environment at

378   ~15 MPa and several hundred Celsius for pressurized water reactors (Office of Nuclear

379   Reactor Regulation, 2012)) or in the Earth's lower mantle (up to 137 GPa and ~4000 K at

380   the core-mantle boundary). We find that, although the cotunnite-type phase of ThO_2 is

381   ~6% denser than its lower-pressure polymorph, they have a very similar compressibilities

382   and thermal pressure coefficients. We also find that the cotunnite structure is

383   continuously deforming under pressure, which suggests that this material will undergo

384   another phase transition on increasing pressure. Such a phase transition has been

385   predicted above ~80 GPa theoretically (Perry et al., 2017). Thus, actinide-bearing oxides

386   in the lowermost region of Earth's lower mantle may not be stable in the cotunnite-type

387   phase. This behavior has the potential to influence the distribution of large ion lithophile

388   elements among accessory phases, particularly if the post-cotunnite structure exhibits a

389   significantly different coordination environment than the cotunnite-type structure.

390

408

409

410   **REFERENCES**
411

412   Akahama, Y., and Kawamura, H. (2007) Diamond anvil Raman gauge in multimegabar

413   pressure range. High Pressure Research, 27(4), 473-482.

414   Arevalo Jr., R., McDonough, W.F., and Luong, M. (2009) The K/U ratio of the silicate
415   Earth: Insights into mantle composition, structure and thermal evolution. Earth
416   and Planetary Science Letters, 278, 361-369.

417   Boettger, J.C. (2009) Theoretical zero-temperature isotherm and structural phase stability
418   of thorium dioxide. International Journal of Quantum Chemistry, 109(15), 3564-
419   3569.

420   Boudjemline, A., Louail, L., Islam, M.M., and Diawara, B. (2011) Dependence of
421   pressure on elastic, electronic and optical properties of CeO2 and ThO2: A first
422   principles study. Computational Materials Science, 50(7), 2280-2286.

423   Boulfelfel, S.E., Zahn, D., Hochrein, O., Grin, Y., and Leoni, S. (2006) Low-dimensional
424   sublattice melting by pressure: Superionic conduction in the phase interfaces of
425   the fluorite-to-cotunnite transition of CaF2. Physical Review B, 74(9), 094106.

426   Boultif, A., and Louër, D. (2004) Powder pattern indexing with the dichotomy method.
427   Journal of Applied Crystallography, 37, 724-731.

428   Campbell, A.J., Danielson, L., Righter, K., Seagle, C.T., Wang, Y., and Prakapenka, V.B.
429   (2009) High pressure effects on the iron–iron oxide and nickel–nickel oxide
430   oxygen fugacity buffers. Earth and Planetary Science Letters, 286(3-4), 556-564.

431   Campbell, A.J., Seagle, C.T., Heinz, D.L., Shen, G., and Prakapenka, V.B. (2007) Partial
432   melting in the iron–sulfur system at high pressure: A synchrotron X-ray
433   diffraction study. Physics of the Earth and Planetary Interiors, 162(1-2), 119-128.

434   Clausen, K.N., Hackett, M.A., Hayes, W., Hull, S., Hutchings, M.T., MacDonald, J.E.,
435   McEwen, K.A., Osborn, R., and Steigenberger, U. (1989) Coherent Diffuse
436   Neutron Scattering From UO2 and ThO2 at Temperatures Above 2000 K. Physica
437   B, 156-157, 103-106.

438   Crowhurst, J.C., Jeffries, J.R., Aberg, D., Zaug, J.M., Dai, Z.R., Siekhaus, W.J., Teslich,
439   N.E., Holliday, K.S., Knight, K.B., Nelson, A.J., and Hutcheon, I.D. (2015) A
440   combined theoretical and experimental investigation of uranium dioxide under
441   high static pressure. Journal of Physics: Condensed Matter, 27(26), 265401.

442   Cuney, M. (2013) Uranium and thorium resources and the sustainability of nuclear
443   energy. In P.C. Burns, and G.E. Sigmon, Eds. Uranium: Cradle to Grave,

444   Mineralogical Association of Canada Short Course Series, 43, p. 417-437.

445   Mineralogical Association of Canada.

446 Dancausse, J.-P., Gering, E., Heathman, S., and Benedict, U. (1990) Pressure-induced

447   phase transition in ThO2 and PuO2. High Pressure Research, 2(5-6), 381-389.

448 Dewaele, A., Belonoshko, A.B., Garbarino, G., Occelli, F., Bouvier, P., Hanfland, M.,

449   and Mezouar, M. (2012) High-pressure–high-temperature equation of state of KCl

450   and KBr. Physical Review B, 85(21), 214105.

451 Dorfman, S.M., Jiang, F., Mao, Z., Kubo, A., Meng, Y., Prakapenka, V.B., and Duffy,

452   T.S. (2010) Phase transitions and equations of state of alkaline earth

453   fluoridesCaF2,SrF2, andBaF2to Mbar pressures. Physical Review B, 81(17).

454 Fonseca, R.O.C., Mallmann, G., Sprung, P., Sommer, J.E., Heuser, A., Speelmanns, I.M.,

455   and Blanchard, H. (2014) Redox controls on tungsten and uranium crystal/silicate

456   melt partitioning and implications for the U/W and Th/W ratio of the lunar

457   mantle. Earth and Planetary Science Letters, 404, 1-13.

458 Haines, J., Léger, J.M., Hull, S., Petitet, J.P., Pereira, A.S., Perottoni, C.A., and da

459   Jornada, J.A.H. (1997) Characterization of the cotunnite-type phases of zirconia

460   and hafnia by neutron diffraction and Raman spectroscopy. Journal of the

461   American Ceramic Society, 80(7), 1910-1914.

462 Idiri, M., Le Bihan, T., Heathman, S., and Rebizant, J. (2004) Behavior of actinide

463   dioxides under pressure: UO2 and ThO2. Physical Review B, 70(1), 014113.

464 Jayaraman, A., Kourouklis, G.A., and Van Uitert, L.G. (1988) A high pressure Raman

465   study of ThO2 to 40 GPa and pressure-induced phase transition from fluorite

466   structure. Pramana - Journal of Physics, 30(3), 22-231.

467 Kamali, K., Ananthasivan, K., Ravindran, T.R., and Kumar, D.S. (2017) High pressure

468   Raman spectroscopic studies on nanocrystalline ThO 2. Journal of Nuclear

469   Materials, 493, 77-83.

470 Kanchana, V., Vaitheeswaran, G., Svane, A., and Delin, A. (2006) First-principles study

471   of elastic properties of CeO2, ThO2 and PoO2. Journal of Physics: Condensed

472   Matter, 18(42), 9615-9624.

473   Klotz, S., Chervin, J.C., Munsch, P., and Le Marchand, G. (2009) Hydrostatic limits of
474   11 pressure transmitting media. Journal of Physics D: Applied Physics, 42(7),
475   075413.

476   Kuksin, A.Y., and Smirnova, D.E. (2014) Calculation of diffusion coefficients of defects
477   and ions in UO2. Physics of the Solid State, 56(6), 1214-1223.

478   Kupryazhkin, A.Y., Svetlichnyi, D.G., and Zhiganov, A.N. (2011) Self-diffusion of
479   oxygen in superstoichiomertric uranium dioxide in the range of the superion
480   phase transition. Technical Physics, 56(2), 221-225.

481   Li, H., Tao, Q., Li, N., Tang, R., Zhao, Y., Zhu, H., Zhu, P., and Wang, X. (2016)
482   Pressure-induced structural transition of Y 2 Zr 2 O 7. Journal of Alloys and
483   Compounds, 660, 446-449.

484   Li, Q., Yang, J.-S., Huang, D.-H., Cao, Q.-L., and Wang, F.-H. (2014) Phase transition
485   and thermodynamic properties of ThO2: Quasi-harmonic approximation
486   calculations and anharmonic effects. Chinese Physics B, 23(1), 017101.

487   Li, S., Ahuja, R., and Johansson, B. (2002) High pressure theoretical studies of actinide
488   oxides. High Pressure Research, 22, 471-474.

489   Macedo, P.M., Capps, W., and Wachtman Jr., J.B. (1964) Elastic constants of single
490   crystal ThO2 at 25°C. Journal of the American Ceramic Society, 47(12), 651.

491   March, N.H., Richardson, D.D., and Tosi, M.P. (1980) Correlation of the superionic
492   transition temperature and Frenkel energy in fluorite crystals. Solid State
493   Communications, 35, 903-905.

494   Matveev, L.V., and Veshchunov, M.S. (1997) High-temperature transition of uranium
495   dioxide to the super-ion state. Journal of Experimental and Theoretical Physics,
496   84(2), 322-329.

497   McDonough, W.F., and Sun, S.-s. (1995) The composition of the Earth. Chemical
498   Geology, 120, 223-253.

499   Nishio-Hamane, D., Dekura, H., Seto, Y., and Yagi, T. (2015) Theoretical and
500   experimental evidence for the post-cotunnite phase transition in zirconia at high
501   pressure. Physics and Chemistry of Minerals, 42(5), 385-392.

502   Office of Nuclear Reactor Regulation. (2012) Standard Technical Specifications Babcock
503   and Wilcox Plants Vol. 1., Washington, D.C.

21

504   Olsen, J.S., Gerward, L., Kanchana, V., and Vaitheeswaran, G. (2004) The bulk modulus
505   of ThO2—an experimental and theoretical study. Journal of Alloys and
506   Compounds, 381(1-2), 37-40.

507   Perry, S.N., Pigott, J.S., and Panero, W.R. (2017) Ab initio calculations of uranium and
508   thorium storage in CaSiO3-perovskite in the Earth's lower mantle. American
509   Mineralogist, 102(2), 321-326.

510   Prakapenka, V.B., Kubo, A., Kuznetsov, A., Laskin, A., Shkurikhin, O., Dera, P., Rivers,
511   M.L., and Sutton, S.R. (2008) Advanced flat top laser heating system for high
512   pressure research at GSECARS: application to the melting behavior of
513   germanium. High Pressure Research, 28(3), 225-235.

514   Prescher, C., and Prakapenka, V.B. (2015) DIOPTAS: A program for reduction of two-
515   dimensional X-ray diffraction data and data exploration. High Pressure Research,
516   35(3), 223-230.

517   Rittman, D.R., Turner, K.M., Park, S., Fuentes, A.F., Yan, J., Ewing, R.C., and Mao,
518   W.L. (2017) High-pressure behavior of A2B2O7 pyrochlore (A=Eu, Dy; B=Ti,
519   Zr). Journal of Applied Physics, 121(4), 045902.

520   Rodriguez-Carvajal, J. (1993) Recent advanes in magnetic structure determination by
521   neutron powder diffraction + FULLProf. Physica B: Condensed Matter, 192(55-
522   56).

523   Ross, M., Mao, H.K., Bell, P.M., and Xu, J.A. (1986) The equation of state of dense
524   argon: A comparison of shock and static studies. The Journal of Chemical
525   Physics, 85(2), 1028-1033.

526   Sevik, C., and Çağın, T. (2009) Mechanical and electronic properties of CeO2, ThO2,
527   and (Ce,Th)O2 alloys. Physical Review B, 80(1), 014108.

528   Shein, I.R., Shein, K.I., and Ivanovskii, A.L. (2007) Elastic and electronic properties and
529   stability of SrThO3, SrZrO3 and ThO2 from first principles. Journal of Nuclear
530   Materials, 361(1), 69-77.

531   Song, H.X., Geng, H.Y., and Wu, Q. (2012) Pressure-induced group-subgroup phase
532   transitions and post-cotunnite phases in actinide dioxides. Physical Review B,
533   85(6), 064110.

534   Toby, B.H., and Von Dreele, R.B. (2013) GSAS-II: The genesis of a modern open-source

535   all purpose crystallography software. Journal of Applied Crystallography, 46(544-

536   549).

537   Wang, B.-T., Shi, H., Li, W.-D., and Zhang, P. (2010) First-principles study of ground-

538   state properties and high pressure behavior of ThO2. Journal of Nuclear

539   Materials, 399(2-3), 181-188.

540   Zhang, F.X., Lang, M., Liu, Z., and Ewing, R.C. (2010) Pressure-induced disordering and

541   anomalous lattice expansion in La2Zr2O7 pyrochlore. Phys Rev Lett, 105(1),

542   015503.

543
544

545   **FIGURE CAPTIONS**

546   **Figure 1. a)** The fluorite crystal structure. **b)** The cotunnite-type crystal structure. Green

547   spheres represent the Th^{4+} cations, red spheres represent the O^{2-} anions.

548   **Figure 2.** Raw diffraction images and integrated diffraction patterns for three *in situ*

549   XRD measurements of sample B25. KBr was the pressure-transmitting medium, thermal

550   insulator, and pressure standard for the experiment. Pt acted as the laser-absorber for the

551   laser heating experiments.

552   **Figure 3.** Room temperature *P-V* data for thorianite from this study and the available

553   literature. The *ab initio* curve from Olsen et al. (2004) was developed using the

554   Generalized Gradient Approximation. The difference between the pressures predicted

555   from calculations and the measured pressure is shown in the bottom panel. The solid line

556   corresponds to the offset in ambient pressure volumes (predicted-measured). A

557   discontinuity is apparent in the data beginning around 15 GPa.

558   **Figure 4.** Raman spectra of ThO_2 collected at room temperature on increasing pressure.

559   Lines indicate the trajectories of peaks with increasing pressure. Colors are coordinated

560   with frequencies plotted in Fig. 5.

561   **Figure 5.** Raman vibrational frequencies as a function of pressure. Thorianite exhibits a

562   single vibrational mode (black triangles), whereas 8 separate peaks were identified for the

563   cotunnite-type phase. Upward solid triangles were measured on increasing pressure,

564   downward open triangles are decreasing pressure. Pressure dependencies were fit to

565   linear trends, which are shown in their corresponding color.

566   **Figure 6.** Phase diagram for ThO_2. Circles indicate in situ XRD measurements. Black:

567   thorianite; green: mixed phase; blue: cotunnite-type ThO_2. Orange X's: low density

568   thorianite determined from Fig. 3 (indicates anion sub-lattice disorder). Triangles indicate

569   relevant Raman measurements. Black: last spectrum with only thorianite; orange: some

570   new vibrational modes observed; green: all high-P modes are present; blue: phase

571   transformation appears complete. The grey shaded region indicates our preferred phase

572   boundary. See text for discussion.

573   **Figure 7.** Measured *P-V-T* data for thorianite and cotunnite-type ThO_2. Curves are

574   isotherms calculated using the equation of state parameters from Table 1. Isotherms are

575   color-coded by temperature. Residuals to the fits are provided in the bottom panels.

576   **Figure 8.** Individual lattice parameters and their ratios for cotunnite-type ThO_2. Black

577   lines are linear fits to the data. No temperature dependence was resolved for the lattice

578   parameter ratios.

579   **TABLES**

580   **Table 1.** Measured and calculated equation of state parameters for the polymorphs of

581   ThO_2. Bold values were held fixed in the fitting procedure. LH = laser-heated; RT =

582   room temperature; FP = full potential; PAW = projector-augmented wave method; PBE =

583   Perdew-Burke-Ernzerhof functional; LCGTO-FF = linear combinations of Gaussian type

584   orbitals-fitting function; LMTO = linear muffin-tin orbital method; LDA = local density

585   approximation; GGA = general gradient approximation; ASA = atomic-sphere

586   approximation; INS = inelastic neutron scattering. This table was adapted from Olsen et

587   al. 2004.

Thorianite					
V_0 (cm³/mole)	K_0 (GPa)	K_0'	αK_T (GPa/K)	Ref.	Method
26.379(7)	204(2)	**4**	0.0035(3)	This study	LH-DAC
26.44	198(2)	4.6(3)		Idiri et al. (2004)	RT-DAC
26.37	262(4)	6.7(5)		Dancausse et al. (1990)	RT-DAC
26.39	195(2)	5.4(2)		Olsen et al. (2004)	RT-DAC
25.36	225	4.2		Olsen et al. (2004)	FP-LMTO-LDA
26.60	198	4.2		Olsen et al. (2004)	FP-LMTO-GGA
26.68	189	4.10		Perry et al. (2017)	GGA-PAW
26.8	191	4.5		Wang et al. (2010)	GGA-PAW
26.33	187.6	4.19		Li et al. (2014)	GGA-PBE
26.77	184.5	4.49		Boettger (2009)	GGA-LCGTO-FF
25.32	225	4.4		Kanchana et al. (2006)	FP-LMTO-LDA

26.58	198	4.5		Kanchana et al. (2006)	FP-LMTO-GGA
26.16	198	4.91		Boudjemline et al. (2011)	GGA
25.53	290			Kelly and Brooks (1987)	LMTO-ASA
26.76	192.8			Shein et al. (2007)	FLAPW
26.44	216			Sevik and Çağln (2009)	LDA+U
	175			Harding et al. (1994)	Dirac-Fock approx.
	221			Li et al. (2002)	FP-LMTO-GGA
	223			Clausen et al. (1987)	INS
	193(2)			Macedo et al. (1964)	Ultrasound
Cotunnite-type ThO₂					
24.75(6)	190(3)	**4**	0.0037(4)	This study	LH-DAC
25.07	177	4.2		Perry et al. (2017)	GGA-PAW
25.1	148	7.8		Wang et al. (2010)	GGA-PAW
24.1	202.1	4.22		Li et al. (2014)	GGA-PBE
24.7	206.8	4.94		Boettger (2009)	GGA-LCGTO-FF
24.55	163.2	6.19		Boudjemline et al. (2011)	GGA

588

589

590 **Table 2.** Pressure dependences of the measured Raman modes for thorianite and
591 cotunnite-type ThO_2. v_0 is the zero-pressure frequency. γ_i are the mode Grüneisen
592 parameters for each vibrational mode, defined as $K_0(d\ln v_i/dP)$.

Raman mode	v_0 (cm^{-1})	dv_i/dP (cm^{-1}/GPa)	γ_i
F_{2g}	460(2)	2.37(9)	0.96(4)
M1	497(3)	1.55(6)	0.51(2)
M2	577(3)	2.04(8)	0.59(2)
M3	294(3)	1.28(7)	0.69(4)
M4	325(4)	1.05(8)	0.54(4)
M5	365(3)	0.83(6)	0.39(3)
M6	465(3)	0.85(7)	0.32(3)
M7	497(3)	1.55(6)	0.41(4)

593

594   **Table 3.** Linear fits to the lattice parameter ratios as a function of pressure for cotunnite-

595   type ThO$_2$.

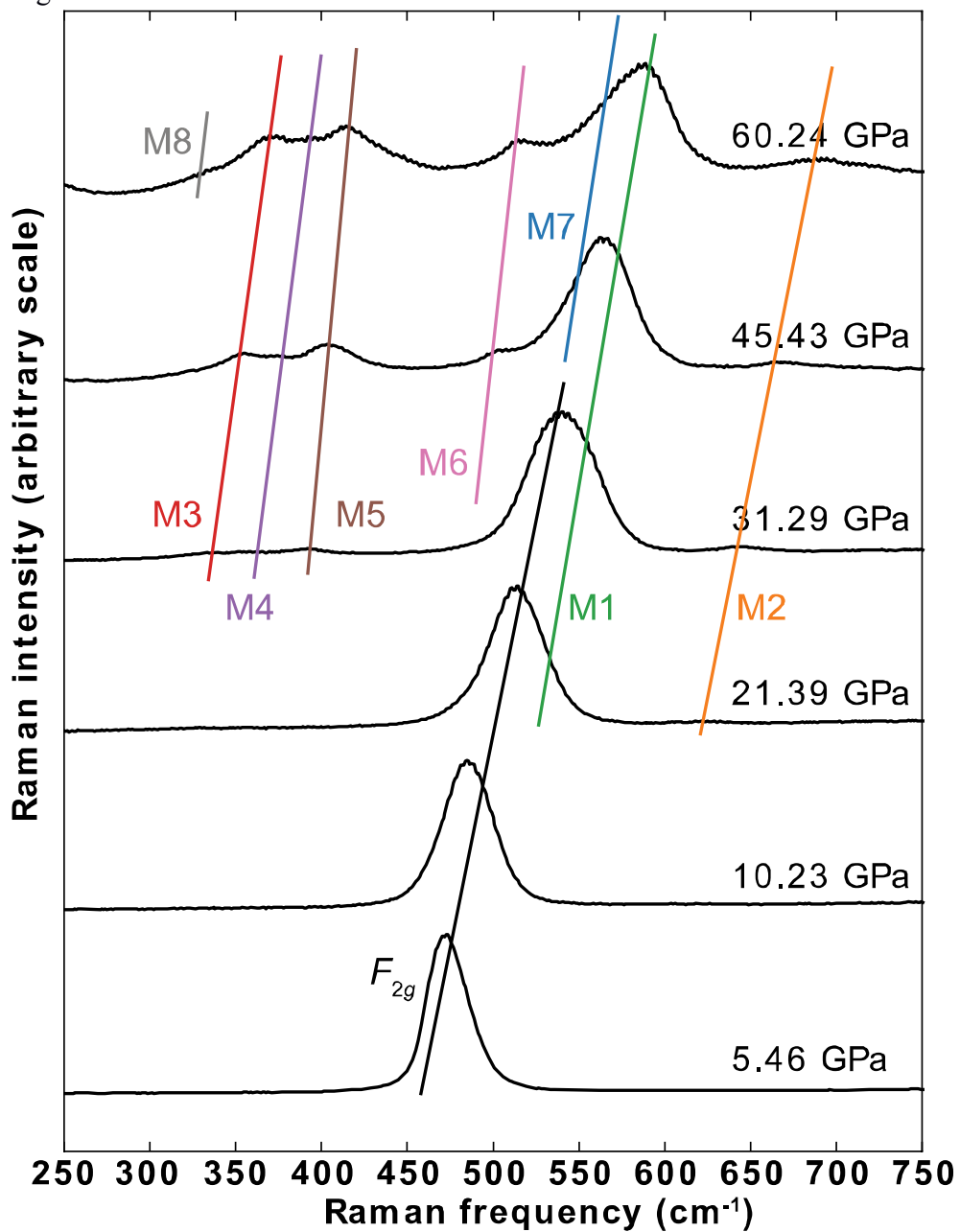| Ratio	Slope (GPa^{-1})	Zero-pressure value
c/a	0.00081(2)	1.1391(9)
b/a	0.00048(2)	0.5962(8)
c/b	-0.00015(3)	1.910(1)

596

597

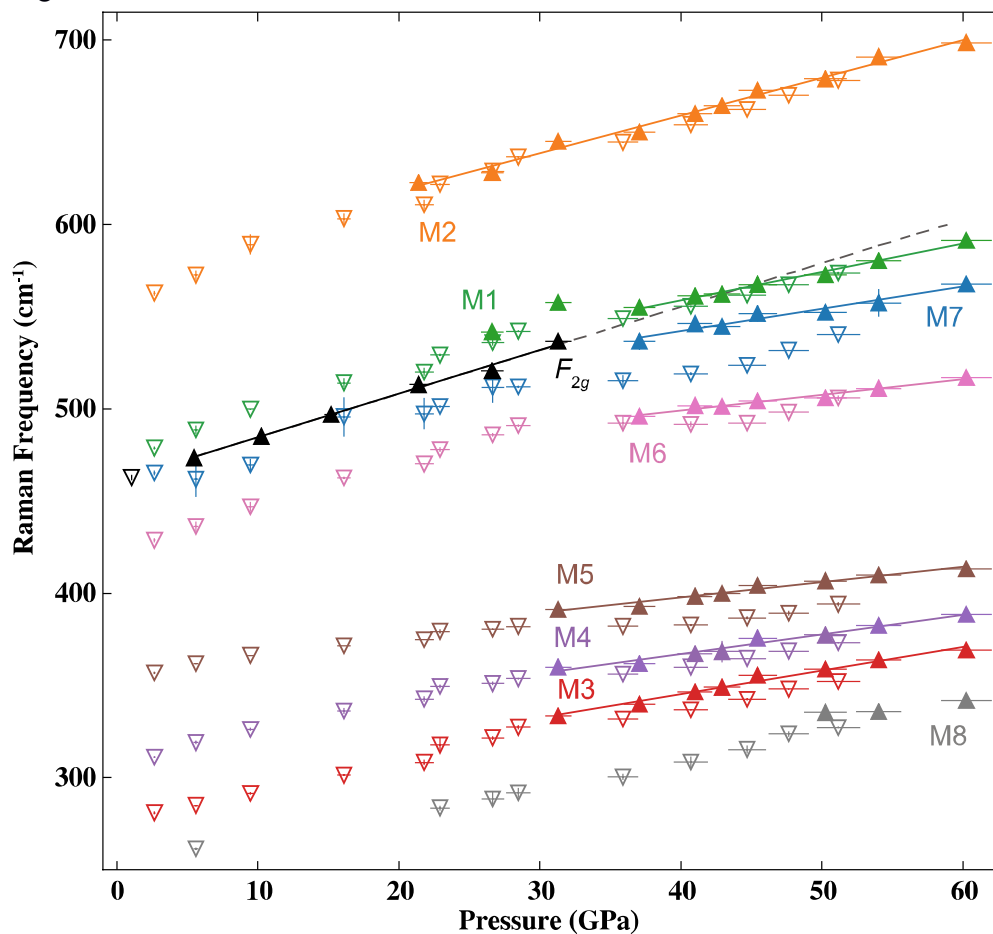598   Fig. 1.
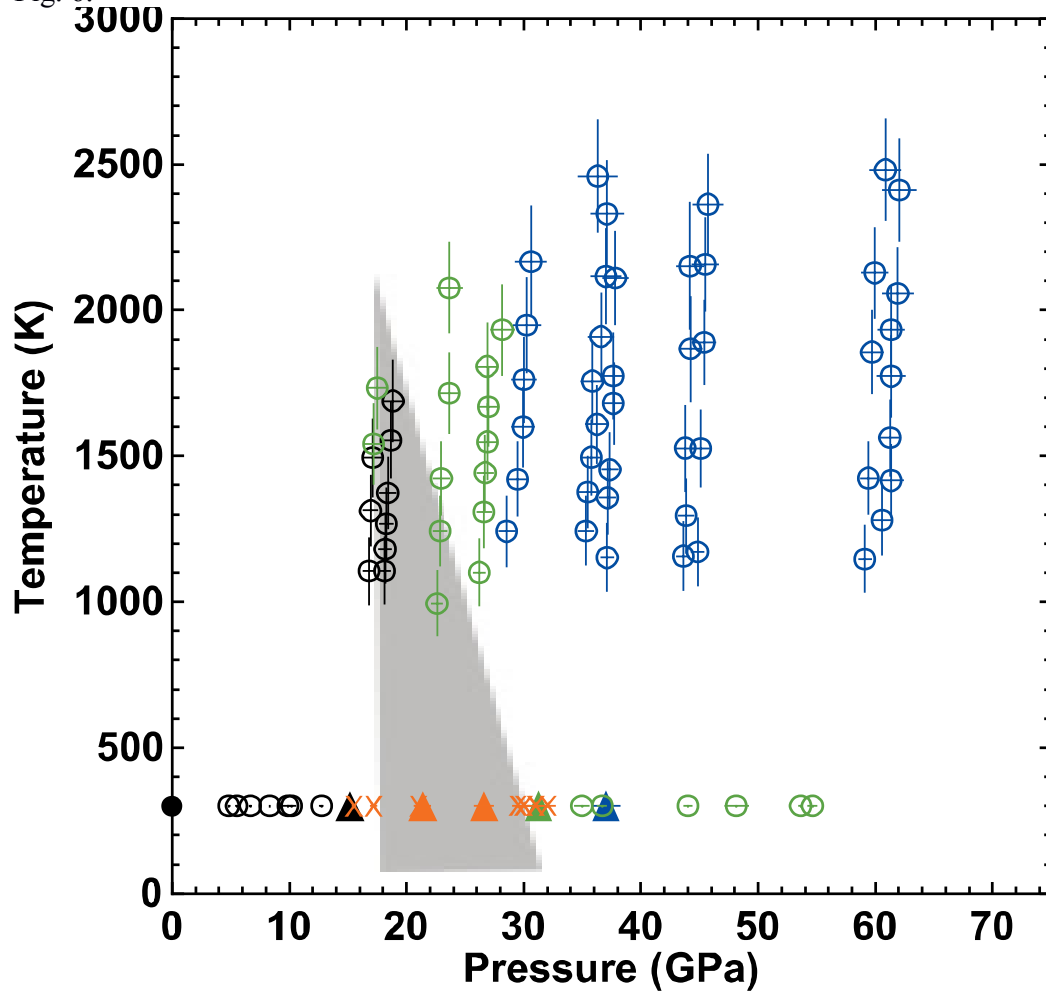

599
600

601   Fig. 2.

602
603
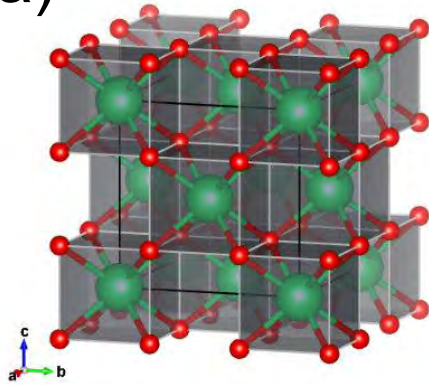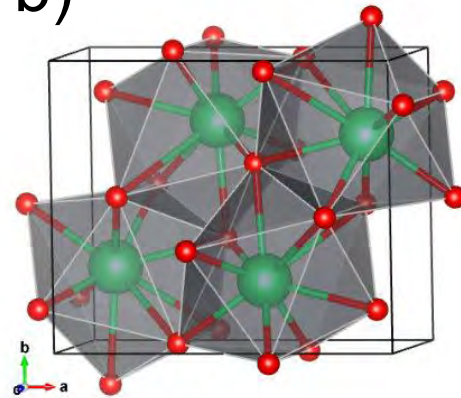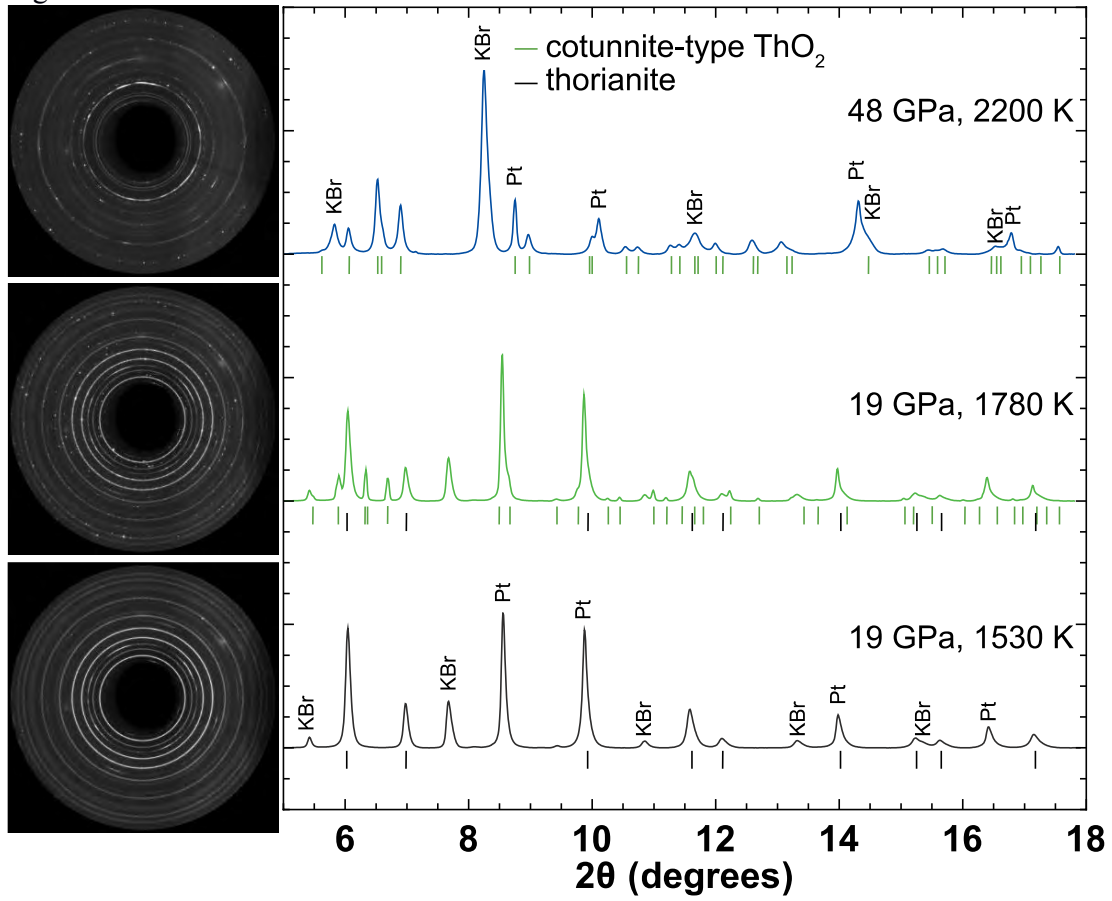
604   Fig. 3.

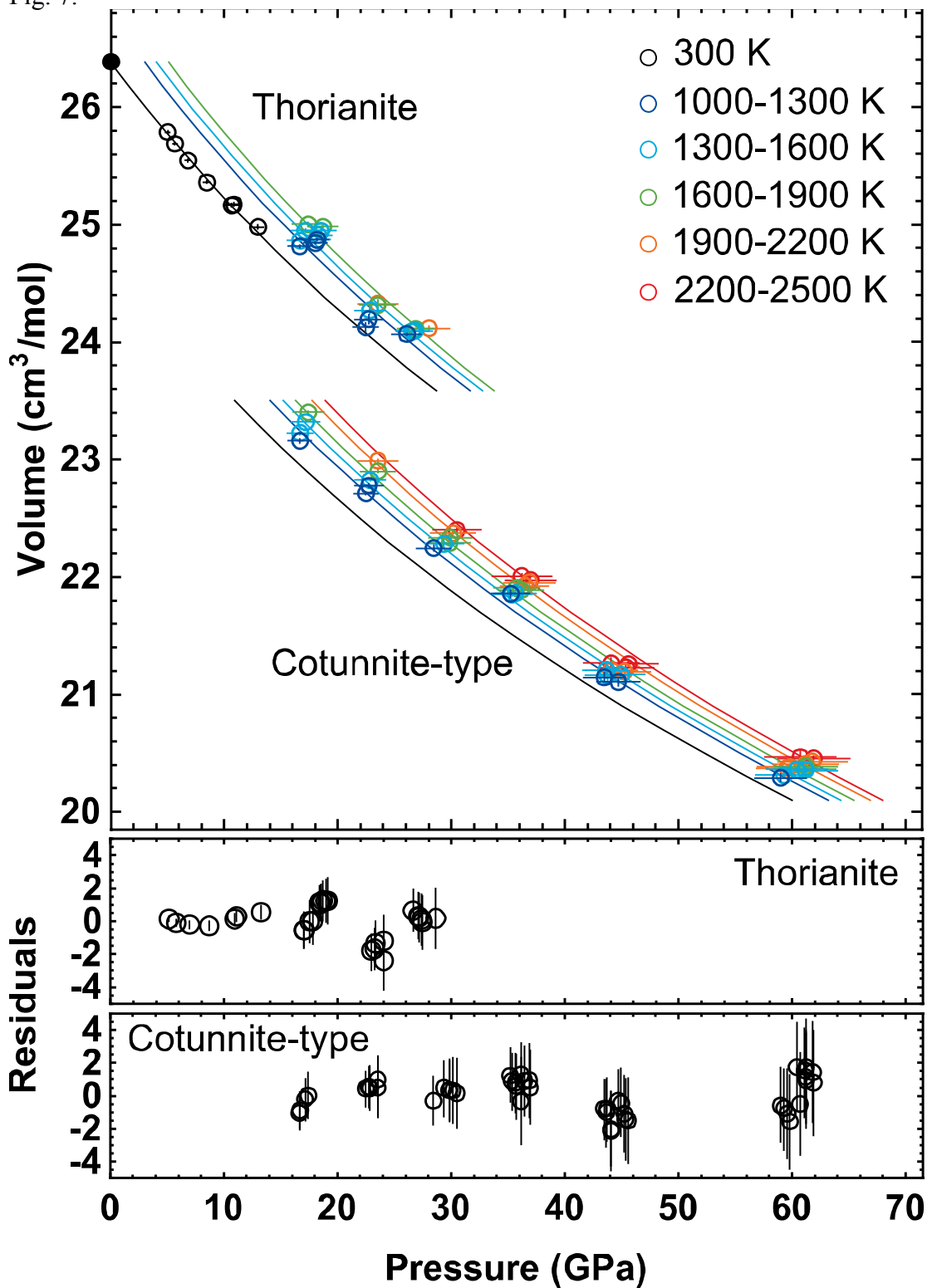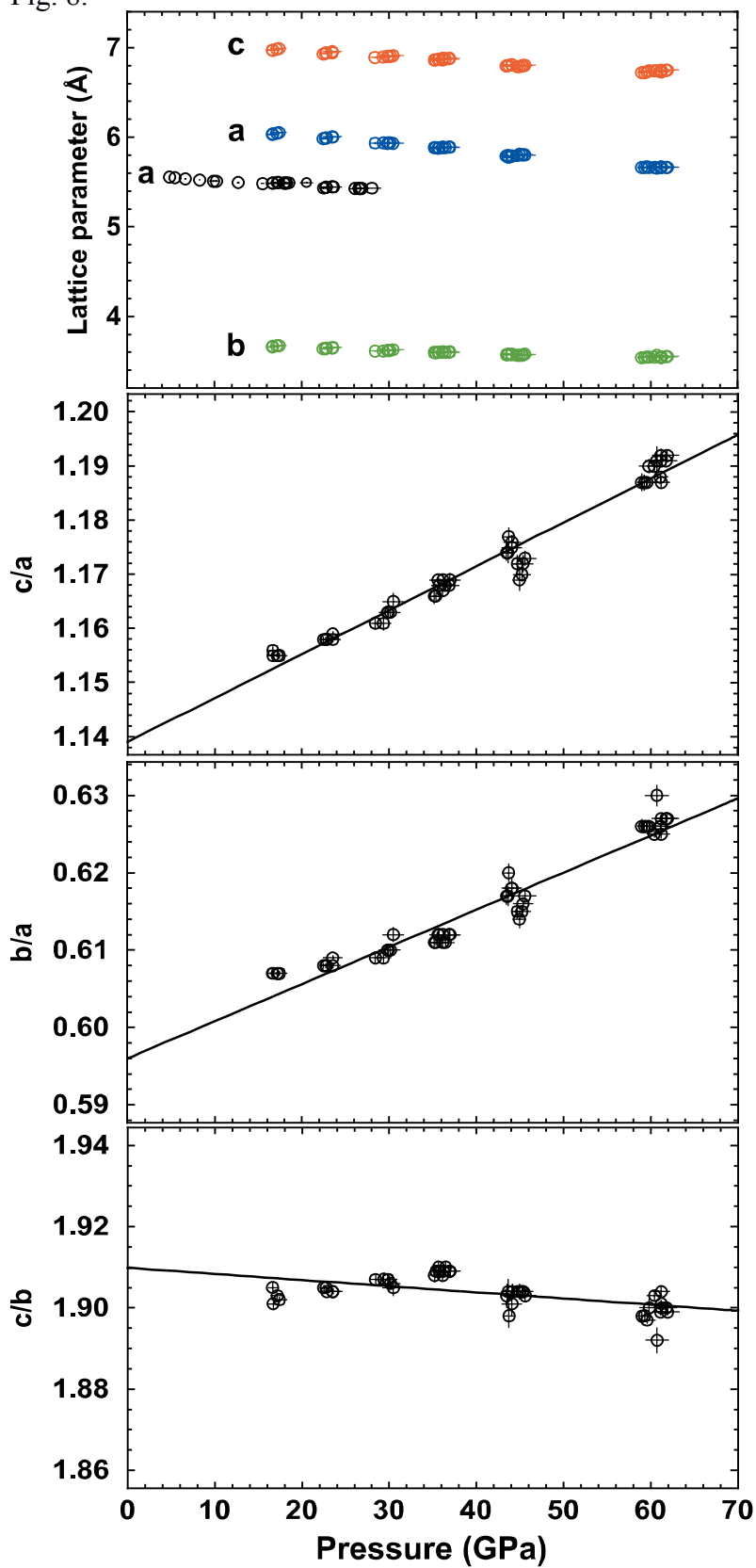605
606

607   Fig. 4.

608
609
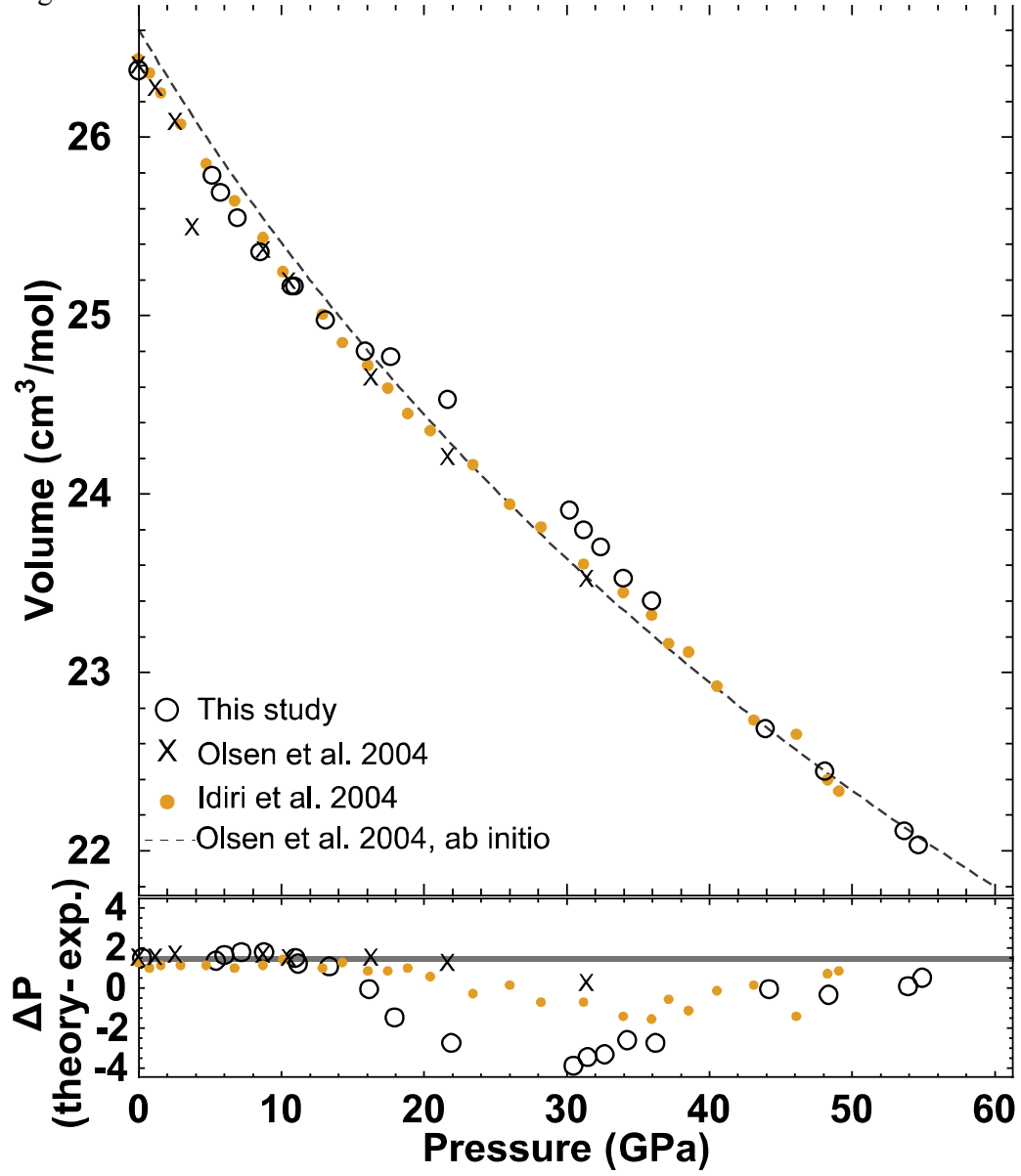
610   Fig. 5.

611
612

613   Fig. 6.

614
615

616   Fig. 7.

617
618

619   Fig. 8.

620